https://doi.org/10.1007/s41230-025-5024-y

Stray grains evolution and high-temperature stress rupture behavior of crystallographic lamellar microstructure in Ni-based superalloys prepared by laser powder bed fusion

Peng Wang[1, 2], **Jing-jing Liang[1], Yu-ping Zhu[1], Wei Song[1], Qiao-lei Li[1], Yi Qiu[5], Ying-ju Li[1], Yi-zhou Zhou[1], Han-lin Liao[3], Lei Shi[4], Li-ming Lei[4], Xiao-feng Sun[1], and *Jin-guo Li[1]

1. Shi-changxu Innovation Center for Advanced Materials, Institute of Metal Research, Chinese Academy of Sciences, Shenyang 110016, China

2. School of Materials Science and Engineering, University of Science and Technology of China, Hefei 230000, China

3. ICB-Lermps, University of Technology of Belfort-Montbelard, 90010 Belfort, France

4. Taihang Laboratory, Chengdu 610213, China

5. School of Materials Science and Engineering, Beijing Institute of Technology, Beijing 100081, China

Abstract: The unique crystallographic lamellar microstructure (CLM) Ni-based superalloys fabricated by laser powder bed fusion (LPBF) exhibits excellent tensile properties. This study aims to investigate CLM's high-temperature stress rupture behavior and use these findings to improve the additive manufacturing process. The result shows that the high temperature-induced intergranular fracture in <110> grain region is responsible for stress rupture failure under both conditions of 760 °C/780 MPa and 980 °C/260 MPa. Among them, the sub-grain boundary fracture occurs only under high temperature and low stress, 980 °C/260 MPa. Due to the severe intergranular fracture induced by stray grains, the stress rupture life is very low under both conditions. According to the finite element simulation, the formation of stray grains stems from the unstable heat flow within the melt pool during the process. In addition, the shorter stress rupture lifetime does not excite a more pronounced dislocation network around the γ′ phase. However, the deformation twins can still be activated inside the <110> grains, so it has excellent plasticity under both test conditions. Finally, this work indicates that the future optimization of CLM by LPBF should focus on eliminating of high-angle grain boundaries in <110> grains.

Keywords: crystallographic lamellar microstructure; Ni-based superalloys; additive manufacturing; mechanical properties

CLC numbers: TG146.1+5 **Document code:** A **Article ID:** 1672-6421(2026)01-045-10

1 Introduction

In the past decade, among various additive manufacturing technologies in the superalloy field, laser powder bed fusion (LPBF) has significant potential for developing complex shape components such as turbine blades due to its high design accuracy enabled by minimal spot size[1, 2]. Unlike conventional wrought or cast routes, the extremely rapid solidification rate (R) in LPBF significantly suppresses elemental segregation and promotes dislocation accumulation in as-built alloys[3, 4]. In addition, the LPBF-build parts experience a top-down temperature gradient (G) and cyclic thermal history, which assemble prominent grain texture and strength anisotropy. It is widely acknowledged that the solidification conditions (G/R) at the liquid/solid interface in LPBF are fundamentally governed by melt pool morphology, which is intricately regulated by laser printing parameters[5, 6]. Consequently, divergent processing conditions give rise to diverse solidification microstructures and corresponding mechanical properties.

*Jin-guo Li

Male, born in 1975, Ph. D., Professor. He mainly engages in the development of superalloys dedicated to additive manufacturing and cast single-crystal superalloys.

E-mail: jgli@imr.ac.cn

**Jing-jing Liang

E-mail: jjliang@imr.ac.cn

Received: 2025-01-29; Revised: 2025-05-22; Accepted: 2025-09-19

In recent years, the crystallographic lamellar microstructure (CLM) in Ni-based superalloys fabricated by LPBF has received widespread attention owing to its unique alternate <001>//BD and <110>//BD-oriented grains. Previous reports have demonstrated that CLM possesses excellent tensile properties in Ni-based superalloys[5-7]. The most substantial contributors to tensile performance of CLM are texture-related strengthening mechanisms, including the Schmid factor, Taylor factor, and stress-transfer coefficient[5]. Besides short-term tensile properties, the superalloy is widely applied in the aviation industry, where it operates in a severe environment characterized by elevated temperatures and long-term stresses[2, 7, 8]. To enhance its high-temperature service capability (a critical requirement for this application), a robust texture coexisting with a directional grain morphology is often essential, which is similar to what is typically observed in the CLM. Hence, it is valuable to further explore the underlying high-temperature stress rupture/creep mechanism of CLM. Previous studies focus on CLM's room temperature tensile or corrosion properties in Inconel 718 alloy, which has a service temperature below 750 °C[5]. In the context of 1,000 °C tensile deformation, the activation of deformation twins within the <110>//BD-oriented lamellar microstructure has been identified as the primary mechanism underlying CLM's exceptional plasticity in our recent research[9]. Furthermore, both literature reports and our own results indicate that the failure mechanism of CLM is attributed to intergranular fracture, which arises from the high-temperature failure caused by transverse high-angle grain boundaries[8, 9]. However, based on the results of the present studies, it is not sufficient to explain the deformation mechanism under different temperatures and stress matching. Accordingly, the fracture and deformation mechanisms of CLM, especially when coupled with stress-rupture tests, remain unclear for superalloy applications. Beyond the fracture and deformation mechanisms, reports on the evolution of stray grains in CLM have also attracted significant attention[10, 11]. Existing research demonstrates that a high temperature gradient can promote the formation of a directional solidification microstructure while suppressing stray grain formation[12, 13]. Yet, whether this phenomenon is applicable to CLM in Ni-based superalloys still requires further investigation. Notably, stray grains are a critical factor influencing the mechanical properties of CLM, particularly under high-temperature service conditions.

This work aims to explore stress-rupture behavior and pave the way for the application and improvement of CLM in superalloys. ZGH451 superalloy is designed for additive manufacturing, and its target service temperature is above 750 °C[14]. The stress rupture behavior of LPBF ZGH451 alloy under two different test conditions was examined. Additionally, complementary characterization techniques were employed to investigate fracture mechanisms. The thermal behavior regarding the evolution of stray grains was revealed by the numerical simulation. This study aims to reveal the formation mechanism of stray grains and the stress rupture behavior of crystallographic lamellar microstructure (CLM). Additionally, it will provide valuable guidance for future efforts aimed at optimizing CLM and enhancing the long-term high-temperature service performance of materials.

2 Experimental method

2.1 Preparation, residual stress relief, and hot isostatic pressing of CLM

A ZGH451 superalloy for additive manufacturing was used in this work. The nominal composition of the gas-atomized powder is given in Table 1. The size distribution of the actual ZGH451 powder ranges from 15 to 55 μm. Additionally, the powder exhibits a spherical shape with few surface satellites, a characteristic that indicates good fluidity. The CLM was prepared using a laser-powder bed fusion GE M2 printer with a high-purity argon gas filling system. The process parameters, including laser power, scan speed, layer thickness, hatch spacing, laser spot diameter, and scanning strategy, were selected based on prior studies[9]. Table 2 presents the detailed process parameters. After the LPBF building, the as-built samples were subjected to the heat treatment (650 °C×10 h/air cooling) for residual stress relief under vacuum conditions. Then, the hot isostatic pressing (HIP) (1,180 °C and 160 MPa for 2 h) was applied to eliminate the pores, microcracks, and other defects.

2.2 High-temperature stress rupture test and microstructure characterization

The high-temperature stress rupture test was conducted utilizing the F-25 creep endurance testing machine and according to GB/T2039-2008. The test samples were extracted from HIP materials with the standard size (Φ2 mm×10 mm). Two

Table 1: Chemical compositions of ZGH451 powder (wt.%)

Al	Ti	Ta	Mo	B	C	Co	Cr	W	Ni
4.6	1.2	5.8	1.5	0.019	0.08	10	7	7	Bal.

Table 2: Process parameters of ZGH451 by LPBF

Laser power (W)	Scan speed (mm·s^{-1})	Hatch spacing (μm)	Layer thickness (μm)	Spot size (μm)
260	1,100	80	30	180

different test conditions (760 °C/780 MPa and 980 °C/260 MPa) were conducted to explore the stress rupture behavior of CLM. At least three samples were tested for each condition to ensure the good repeatability of the stress rupture responses.

A field emission scanning electron microscope (SEM) was used to analyzed the stress rupture fracture morphology. Before the SEM test, the specimens were prepared by mechanical grinding and polishing. After that, the ultrasonic cleaning machine was employed to remove dirt from the surface of the sample, and then etching with a mixed solution of HCL (45vol.%) + $CuSO_4$ (8vol.%) + H_2O (45vol.%) + H_2SO_4 (2vol.%) for 15 s.

Electron backscattered diffraction (EBSD) was employed to determine the sample's crystallographic orientation, grain boundary distribution, and dislocation density before and after the stress rupture test. The preparation of EBSD samples consisted of two steps: mechanical grinding through the conventional method and then electro-polishing with $HCLO_4$:C_2H_5OH (1:9) solution at 20 V/−10 °C for 10 s. EBSD measurements were carried out at magnification from about 50 to 500 times with a step size of 1.8 μm. The Aztec and OIM softwares were used to identify all obtained data.

Transmission electron microscopy (TEM) (FEI Talos F200X) was applied to examine high-temperature stress rupture-induced microstructural variations. The TEM samples were obtained via wire-electrode cutting at a position about 5 mm from the fracture surface. The 500 μm metal sheet was mechanically ground to 50 μm, then subjected to dual-jet electro-etching at 40 V/−25 °C with the solution ($HClO_4$: CH_3COOH = 1:4) for about 120 s.

2.3 Numerical simulation

3D finite element modeling was employed to simulate melt flow, with self-built software adopted in the modeling process. The numerical model took into account microscopic fluid forces, including surface tension, Marangoni force, and recoil pressure. It was assumed that the flow of the melt behaved as a laminar flow of a Newtonian fluid. In the discrete element method (DEM) simulation, the translational and rotational motion of each particle was governed by Newton's second law:

$$m_i \frac{\mathrm{d}v_i}{\mathrm{d}t} = F_i + m_i g \tag{1}$$

$$I_i \frac{\mathrm{d}w_i}{\mathrm{d}t} = T_i \tag{2}$$

where m_i, v_i, ω_i, and I_i are the mass, translational velocity, angular velocity, and movement of inertia, respectively; F_i and T_i represent the total force and the total torque acting on the particle i.

The normal contact force (F_n) between particles can be expressed by:

$$F_n = \frac{4E^*}{3R^*} r^3 - 4\sqrt{\pi r^3 \gamma E^*} \tag{3}$$

where r, γ, E^*, and R^* are the radius of the powder particle, the surface energy, the equivalent Young's modulus, and the equivalent contact radius, respectively.

The simulation of the powder melting process was conducted using mass, momentum, and energy conservation equations:

Mass:

$$\nabla \cdot (\rho \vec{v}) = 0 \tag{4}$$

Momentum:

$$\frac{\partial}{\partial t}(\rho \vec{v}) + \nabla \cdot (\rho \vec{v} \times \vec{v}) = \nabla \cdot (\mu \nabla \vec{v}) - \nabla p + \rho \vec{g} \tag{5}$$

Energy:

$$\frac{\partial}{\partial t}(\rho h) + \nabla \cdot (\rho \vec{v} h) = q + \nabla \cdot (k \cdot \nabla T) \tag{6}$$

where $\vec{v}$ and $\vec{g}$ are the velocity vector and gravitational acceleration vector, respectively. t represents time, p is the pressure, ρ is the density, μ is the average viscosity, q is the Gaussian heat source, h is the enthalpy, k is the thermal conductivity, and T is the temperature. The metal powder bed was established using the discrete element method with a 1,000 μm×400 μm×200 μm simulation size. Thermal simulations were run to extract the temperature and fluid flow profiles during the whole process. In the present work, only a simulation domain of size 1,000 μm×400 μm×200 μm was defined and meshed due to the limited effective zone. The adopted mesh was set to 5 μm in the entire computational domain. Single-layer with three-travel scanning was performed to consider the overlapping rate between molten pools on CLM grain boundary formation. The laser heat flux was imposed at the top surface of the sample as a 3D Gaussian distribution. Radiation effects were also considered in the exact location using an emissivity of 0.8. Convective heat transfer operated on the free surfaces of the sample except the bottom one, which was fixed through a heat convection coefficient of 10 $W \cdot (m^2 \cdot K)^{-1}$. All surfaces were set with continuous boundary conditions (zero normal derivative). The powders and the substrate were assumed to be made of the same material, and the gas phase was not included in this analysis.

3 Results and discussion

3.1 Stray grains evolution

The longitudinal section [parallel to the building direction (BD)] microstructure of the CLM after HIP was evaluated via EBSD and TEM. As depicted in Fig. 1(a), the samples exhibit a prominent alternant <001>//BD and <110>//BD grains characteristic. It is worth noting that the CLM consists not only of the above two oriented grains but also contains some other oriented grains, such as <111>//BD grains. Previous reports showed that these non-CLM orientation grains are stary grains and arise from heat flow fluctuation of melt pool[10, 15].

Figure 2 shows the evolution of temperature and flow fields during CLM printing. The model validation is confirmed by comparing the size of the melt pool in the simulations and experiments [Fig. 2(a)]. In CLM, the <001>//BD grains developed in the center of the molten pool due to stable upside temperature gradient (G) promotes solid-liquid interface migration along BD. Such a heat flux condition originates from the flat bottom of the molten pool, which laser process

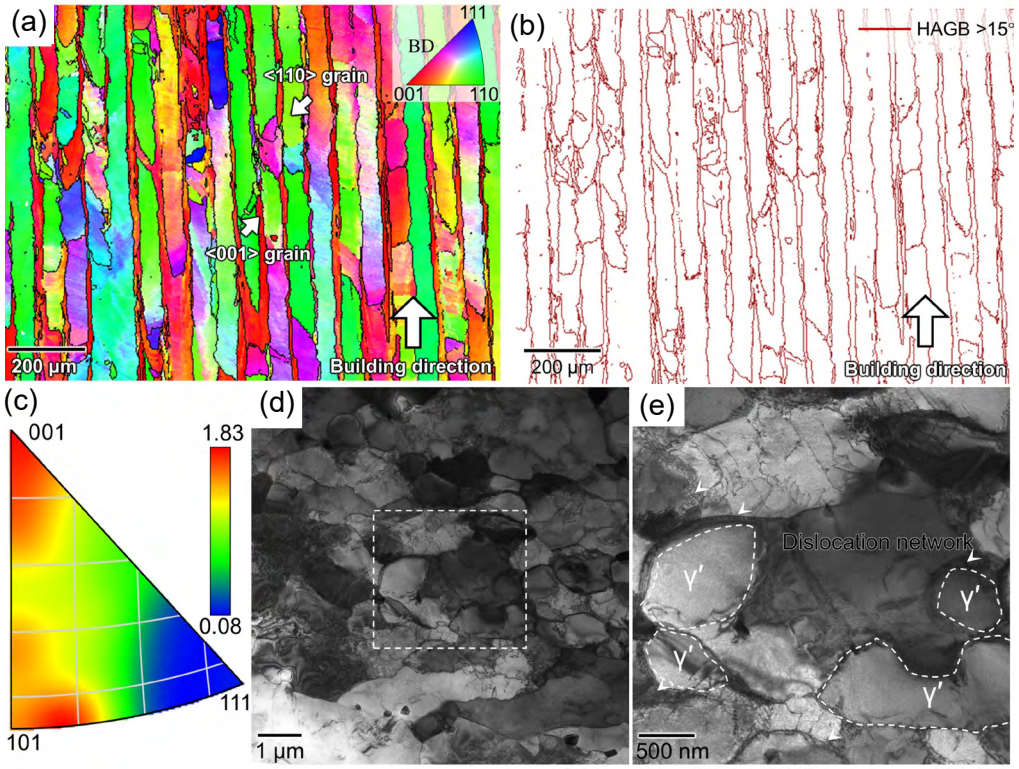

Fig. 1: Microstructure of CLM sample after HIP: (a) texture distribution of *Y-Z* plane; (b) grain boundary distribution corresponds to (a); (c) inverse pole figures; (d) low-magnification TEM image of dislocation distribution; (e) low-magnification TEM image of γ′ phase

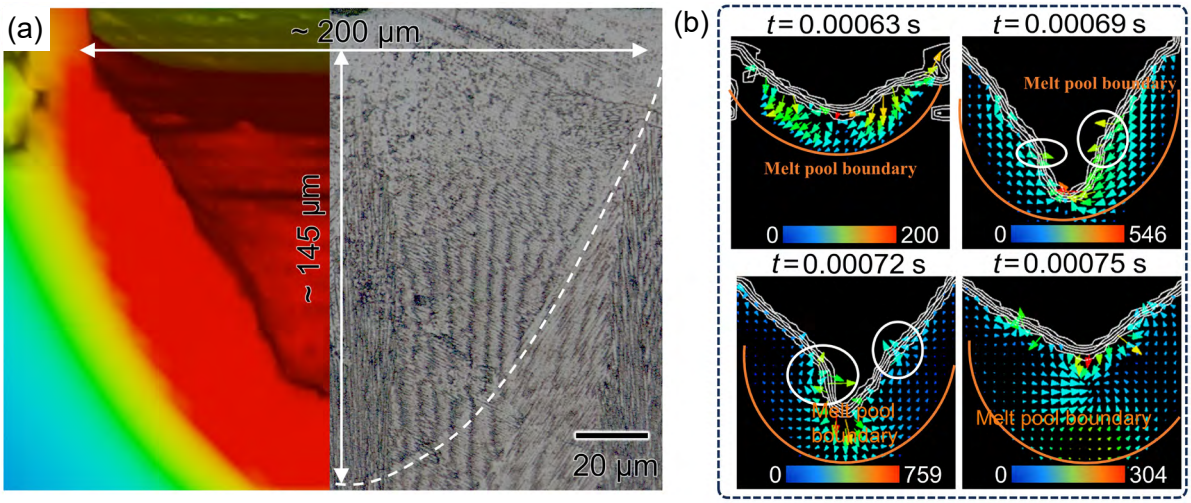

Fig. 2: Comparison of experimentally measured and simulated melt pool size (a) and heat flow evolution (b)

parameters can manipulate[16, 17]. Generally, higher laser power and lower scanning speeds are more conducive to forming CLM. The simulation results indicate that the melt flow in the melt pool, achieved with higher power, is more stable. The energy of the face-centered cubic system is the lowest when the remelted dendrites grow perpendicular to each other[18, 19]. The overlap rate of both neighbor shallow key-hole type melt pools dominates the formation of <110>//BD grains.

As seen in Fig. 2(b), the unstable heat flow at the overlapping molten pool causes nucleation disorder and interruption of epitaxial growth (white circle). These undesired orientation grains usually occur in <110>//BD grains and are the source of transverse grain boundaries. The high angle grain boundaries (HAGB) distributed in CLM, as shown in Fig. 1(b), correspond to IPF in Fig. 1(c). The results reveal numerous transverse grain boundaries within the <110> grains, which are expected to deteriorate long-term high-temperature performance. More microscopic analysis in Fig. 1(d) exhibits many dislocations within these grains. The above phenomenon indicates that the thermal stress inherent in LPBF and subsequent HIP treatment may lead to the accumulation of dislocations in the samples[12]. Following HIP treatment, the coarse γ′ phase precipitates as a result of high-temperature thermal effects. Upon detailed observation, an uneven

dislocation network is found to surround the γ′ phase. Under thermal activation, various modes of dislocation movement, including slip, cross slip, climb, and Orowan, transit the γ′ phase, which may eventually form a dislocation network configuration[13, 15-16]. These dislocation networks in the initial microstructure play an important role in delaying the dislocation movement and improving the strength of the alloy. The tensile strength of the CLM alloy has been proven to be very excellent in different temperature conditions. However, the mechanical performance and fracture mechanism under long-term high-temperature stress remain to be further explored.

3.2 High temperature stress fracture properties

Figure 3 illustrates the stress-rupture life of the CLM samples under conditions of 760 °C/780 MPa and 980 °C/260 MPa. The average stress-rupture life of the CLM after HIP in 760 °C/780 MPa is ~9.66 h, which is significantly higher than 980 °C/260 MPa condition (~2.22 h). Although there is a decrease in stress value from 780 MPa to 260 MPa, the increase in test temperature from 760 °C to 980 °C causes a significant reduction in stress-rupture life. The CLM sample at 980 °C/260 MPa shows better stress-rupture plasticity (20%) than that at 760 °C/780 MPa (13.66%).

3.3 Fracture morphology

Figures 4(a, b) show the fracture morphology of the CLM samples under both test conditions, and the samples have no apparent necking phenomenon. Upon closer inspection [Figs. 4(c, d)], distinct grain boundary cracking appears in <110> grains interior and the interface between <001> and <110>-orientation grains. The disordered atoms weaken the grain boundaries at high temperatures[17]. Therefore, high-temperature long-term stress rupture tests invariably break along grain boundaries. Nevertheless, there are still

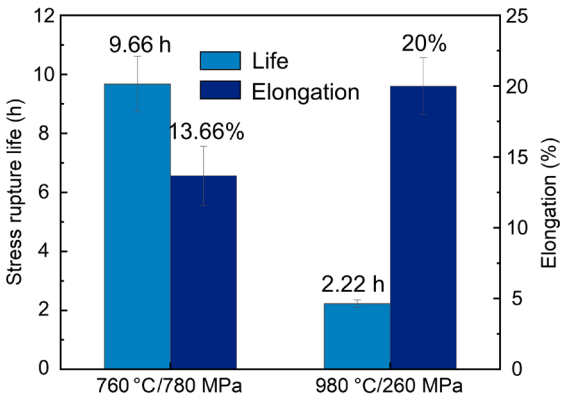

Fig. 3: Stress rupture characteristics of CLM samples under both high-temperature test conditions

some differences in the mode of fracture under both test conditions. The sample under the condition of 760 °C/780 MPa shows a prominent cleavage plane [Fig. 4(c)], which demonstrates that the CLM sample includes intragranular sliding under high temperature and high stress. In addition, vast dendrite is distributed on the fracture surface [Fig. 4(c)], indicating sub-grain failure plays an essential role in stress rupture. In contrast, no evidence of dendrite morphology, and high-temperature oxidation is observed during the 980 °C/260 MPa stress-rupture process.

The longitudinal section of the fracture further verifies the above analysis and clarifies the fracture mode (Fig. 5). Comparing Figs. 5(a) and (b), there is only one long stripe crack in the former case and more in the latter. This indicates that cracking along HAGB possibly does not cause failure at 760 °C/780 MPa condition. It is anticipated that sub-grain cracking is the dominant failure mechanism, which accords with the above analysis. On another condition, the high temperature of 980 °C seriously damages the stability of grain

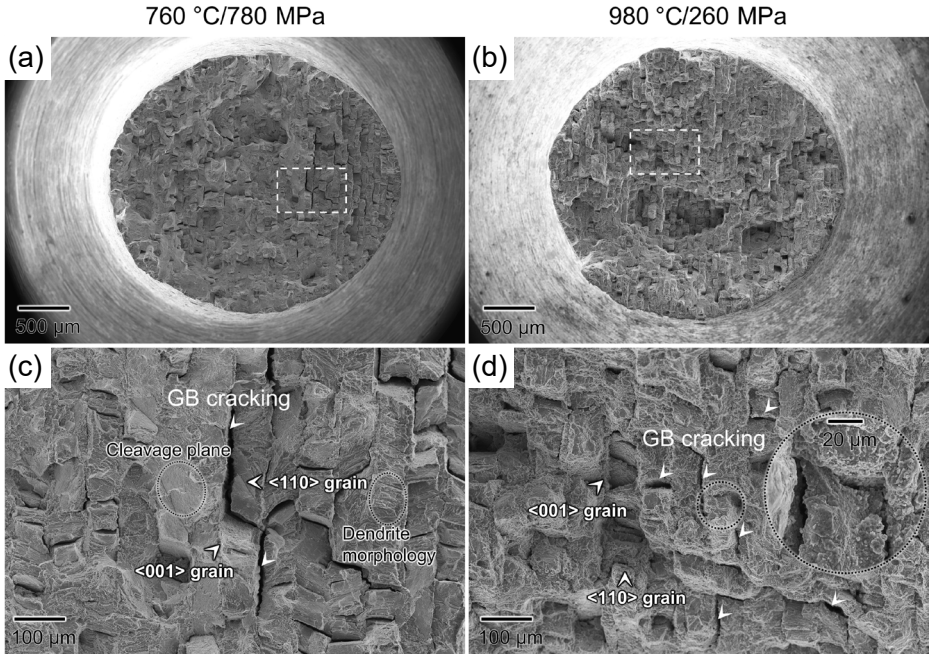

Fig. 4: Cross section of SEM fractography of CLM samples after stress rupture test: (a, c) 760 °C/780 MPa; (b, d) 980 °C/260 MPa

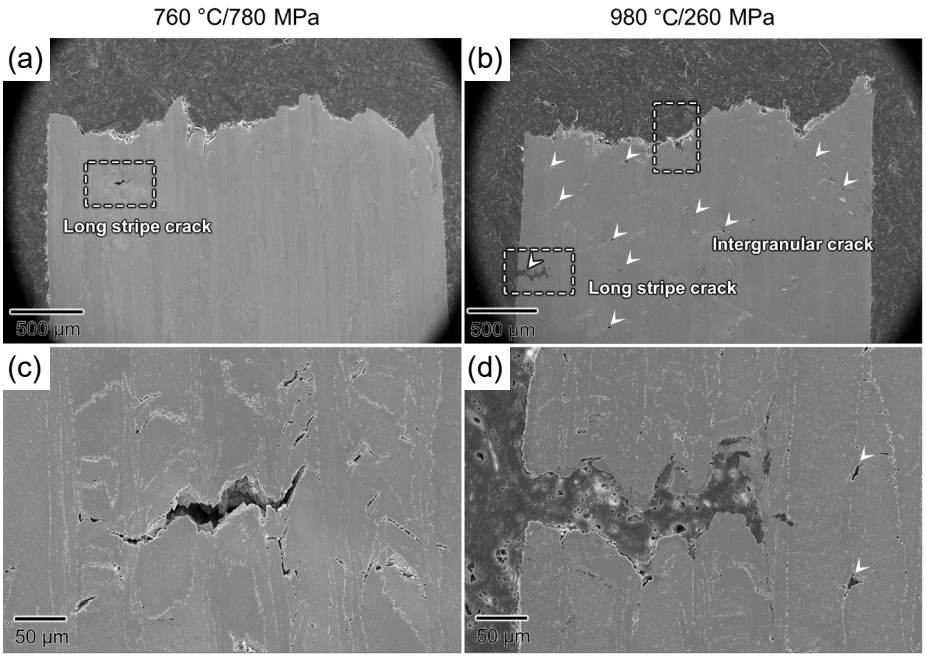

Fig. 5: Longitudinal section of SEM fractography of CLM samples after stress rupture test: (a, c) 760 °C/780 MPa; (b, d) 980 °C/260 MPa

boundaries, and 260 MPa stress accelerates crack initiation and propagation. When intergranular cracks develop long stripe cracks at the border of the test sample [Fig. 5(d)], it is easy to cause a catastrophic stress fracture. Hence, the high-temperature and low-stress specimens exhibit a 77% decrease in stress rupture life. At the same time, the scanning electron microscopy of the longitudinal section cannot determine the origin of these cracks. Other characterization technique is needed to further understand the cracking details.

Figures 6(a, b) show the IPF orientation maps of the only long stripe crack and surrounding micro-cracks at the fracture after the 760 °C/780 MPa test. As seen in Fig. 6(a), the grain boundary cracking can easily be identified between different oriented grains. The geometrically necessary dislocation (GND) density reflects the local misorientation angle θ caused by deformation. Figure 6(c) demonstrates that almost all the crack locations exhibit a certain degree of stress concentration, and the average GND density value is approximately 2.27×10^{14} m^{-2}. Notably, a significant density of deformation twins is activated within <110>//BD-oriented grains, whereas no twin features are detected in <001>//BD-oriented grains. Previous studies show the grain orientation closer to <111>//BD will experience a more significant crystallographic shear, that is, Taylor factors M>2.6[18, 20]. As depicted in Fig. 6(c), the corresponding TF maps demonstrate the <110>//BD-oriented grains have a higher Taylor factor value (~3.22), which have experienced a stronger shear stress. Upon closer examination in the dashed box in Fig. 6(a), these deformation twins can be tens of microns in size. The deformation twins are also identified in the <110>-oriented grains, as confirmed by the orientation maps [Fig. 6(d)]. According to Figs. 6(e, f), the stray grains and interface between <001> and <110> are considered as possible crack sources, which exhibit somewhat dislocation accumulation.

Figure 7(b) displays IPF maps after the 980 °C/260 MPa stress rupture test, corresponding to the dashed box in Fig. 7(a) on the fracture surface. Evidently, multiple intergranular cracks are observed within <110>//BD-oriented grains. Based on the above analysis, these cracks are the primary cause of failure. Similarly, deformation twins are still observed inside <110>//BD-oriented grains [Figs. 7(b, d)], even though the stress rupture life under this condition is only 2.66 h. The relationships between the Taylor factor value and the location of deformation twins are similar to that at 760 °C/780 MPa. However, compared to the 760 °C/780 MPa case, the sample under 980 °C/260 MPa stress rupture exhibits a higher GND density at both low and high magnification. There are two reasons can be responsible for such GND distribution: on the one hand, better plasticity can result in more dislocation accumulation, and on the other hand, more intergranular cracks accumulate a large number of dislocation entanglements in the vicinity[21].

Based on the above results, the CLM samples exhibit a high-temperature stress rupture life-plasticity trade-off under the two different service conditions. Analysis of the fracture morphology reveals that transverse grain boundary cracking decreases stress rupture life at 980 °C/260 MPa. However, the differences in plasticity still need to be further elucidated by other complementary characterization. TEM was used to observe the microstructure near the fracture surface after both deformation conditions (Fig. 8). It is apparent that a significant number of dislocations are formed in matrix channels and bypass the γ′ precipitates under both 760 °C/780 MPa and 980 °C/260 MPa. The mechanical performances of nickel superalloy are closely related to the characteristics of γ′ strengthening phase, including its size, volume fraction, and morphology[20, 22]. In this study, the CLM sample subjected to HIP treatment exhibits an accelerated diffusion rate of elements

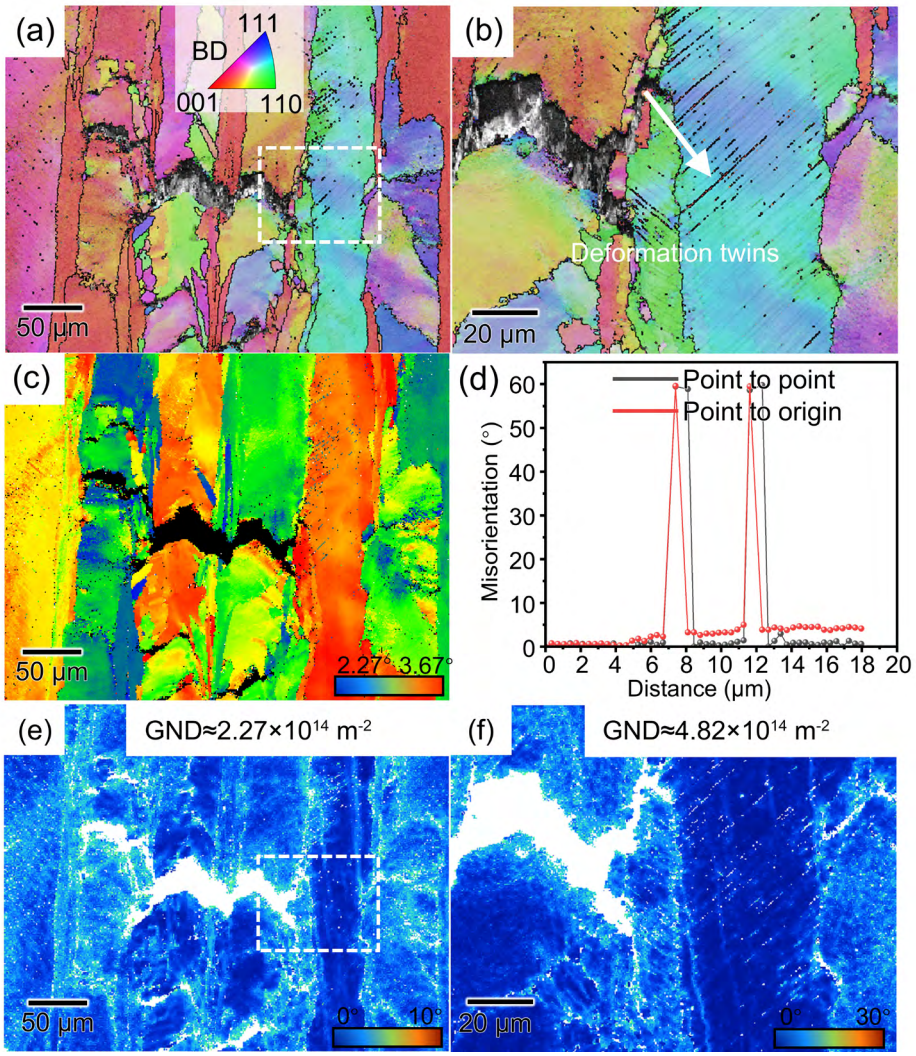

Fig. 6: EBSD images after 760 °C/780 MPa stress rupture test: (a) low-magnification IPF image of crack distribution; (b) high-magnification IPF image of deformation twins; (c) Taylor factor mapping corresponds to (a); (d) plots of misorientation angle variation–measured both point-to-point and cumulatively along the black lines marked in (b); (e, f) GND distribution around stress rupture cracks corresponds to (a, b)

including Ni, Al, and Ta. Although many reports show the as-built alloy in LPBF predominantly features no precipitates due to the rapid solidification process[4, 21], the elevated temperature HIP allows precipitation and coarsening of primary γ′ phase [Fig. 1(e)]. Therefore, some γ′ phases even display an irregular shape, revealing the occurrence of Ostwald ripening [Fig. 1(e)]. As the γ′ phase coarsens, the spacing between them widens. This greater spacing allows dislocations to slip more easily through the channels formed between the γ′ phases, resulting in a decrease in the stress required to bypass them. Consequently, the sample can undergo plastic deformation under a relatively low external force, which is observed macroscopically as an increase in the metal's plasticity. In the HIP CLM sample, besides the coarse γ′ phase, the stress rupture test under both high-temperature conditions further intensifies γ′ ripening[22, 23]. Comparing Figs. 8(a) and (b), the γ′ ripening appears significantly more severe at 980 °C/260 MPa than at 760 °C/780 MPa, leading to a larger γ′ size. However, following the coarsening of the γ′ phase, its compatibility with the γ matrix diminishes during the deformation process. Due to the differing mechanical properties of the γ′ phase and the γ matrix, stress concentration is more likely to occur around the roughened γ′ phases. When this stress concentration reaches a critical level, it can trigger the formation of microcracks. The presence and growth of these microcracks can accelerate material failure and reduce its stress fracture life. Although the stress rupture life significantly decreases at 980 °C/260 MPa, higher temperatures are crucial in increasing γ′ size, contributing to more substantial atoms' diffusion dynamics[23]. The ripening of γ′ phase widens the channels with γ matrix, facilitating dislocation slip. The above EBSD results confirm that GND density is higher at 980 °C/260 MPa than 760 °C/780 MPa. Hence, under 980 °C/260 MPa, the behavior of γ′ phase is more conducive to stress rupture plastic of CLM.

Besides the dislocation slip, the deformation twins are also activated in both conditions, as confirmed by Figs. 6(a) and 7(a). However, due to the enhanced dislocation pile-up and TEM technology limitations, the twins need additional careful observations at 980 °C/260 MPa. Normally, the deformation twins can serve as a barrier to dislocation slip in {111} plane

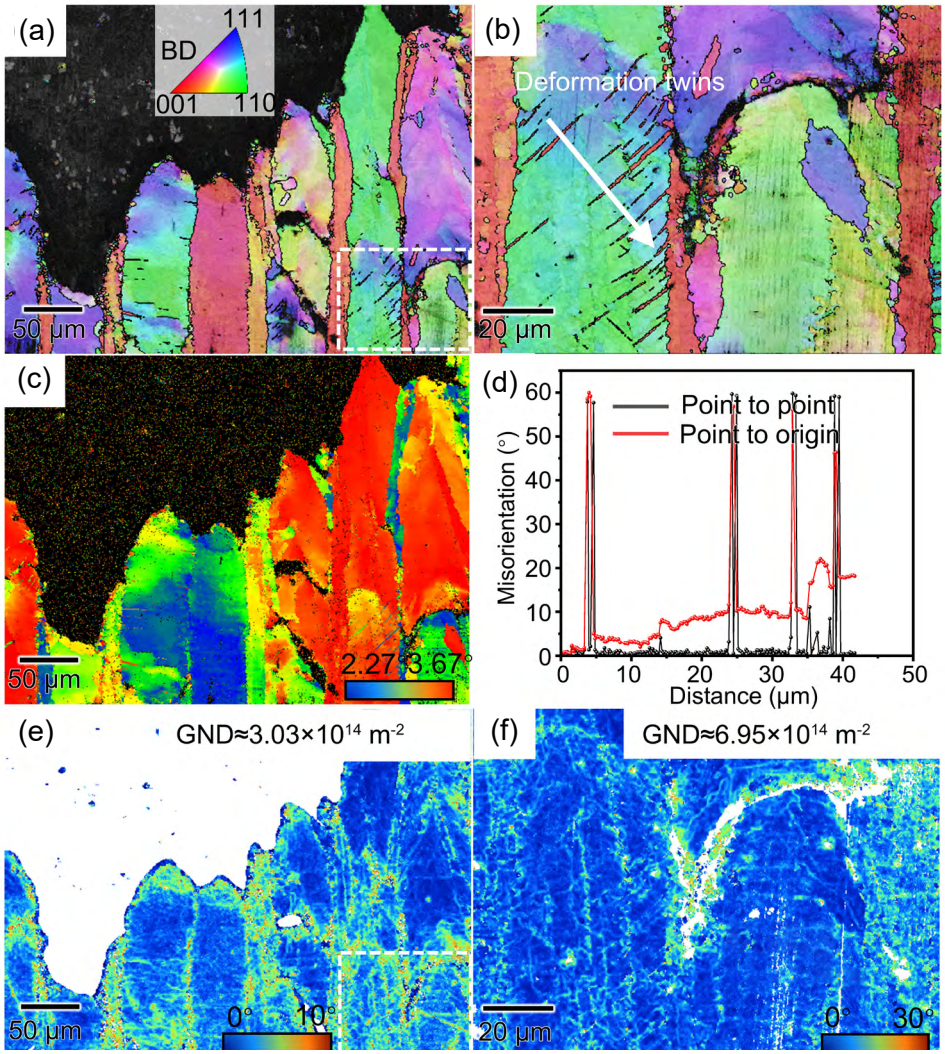

Fig. 7: EBSD images after 980 °C/260 MPa stress rupture test: (a) low-magnification IPF image of crack distribution; (b) high-magnification IPF image of deformation twins; (c) Taylor factor mapping corresponds to (a); (d) plots of misorientation angle variation–measured both point-to-point and cumulatively along the black lines marked in (b); (e, f) GND distribution around stress rupture cracks corresponds to (a, b)

and provide extra strain hardening [Fig. (8b)][24]. The evolution mechanism of deformation twins in CLM can be found in our previous work[9]. In this study, deformation twins are greatly activated in <110>//BD-oriented grains due to the alloy's high flow stress and low stacking fault energies (SFEs)[25]. Hence, the contribution of deformation twins to plastic difference is negligible in both 760 °C/780 MPa and 980 °C/260 MPa conditions.

According to the above analysis, the microstructure of CLM after HIP experiences a thermodynamic coupling and forms the narrow dislocation network in the γ channels [Fig. 1(e)]. It is noteworthy that this dislocation network around the γ′ phase is observed after the 980 °C/260 MPa stress rupture test, while such a network is not apparent after the 760 °C/780 MPa stress rupture test. There are two possible reasons for the initial dislocation network vanishing at 760 °C/780 MPa. On the one hand, a significant number of dislocations are generated in γ channels, which cover the initial dislocation network. On the other hand, under thermal activation, the tangled dislocation networks dissolve and disappear at different slip planes. In general, the formation of dislocation networks is related to activating multiple slip systems[16]. The different glide planes provide a platform for the dislocation interaction, promoting the evolution of the dislocation network. Under the 980 °C/260 MPa stress rupture test, the higher temperature forms an irregular dislocation network around γ′ phase. Previous reports demonstrate that rearranging arrays of dislocations to create a network lowers the energy of tangled dislocations and favors further plastic deformation. Moreover, the dislocation network increases the resistance of dislocation slip and enhances the strain hardening of CLM during plastic flow.

In summary, the high-temperature stress rupture life is not ideal due to the existence of sub-grain boundaries induced by the LPBF process. In addition, the high-angle grain boundaries derived from heat flux fluctuation are also detrimental to the mechanical properties, and we will strive to optimize them in future work. The chaotic heat flow and the irregular overlapping of the molten pool result in transverse grain boundaries in <110>-oriented grains. Importantly, the low-stress fracture life prevents the formation of a regular

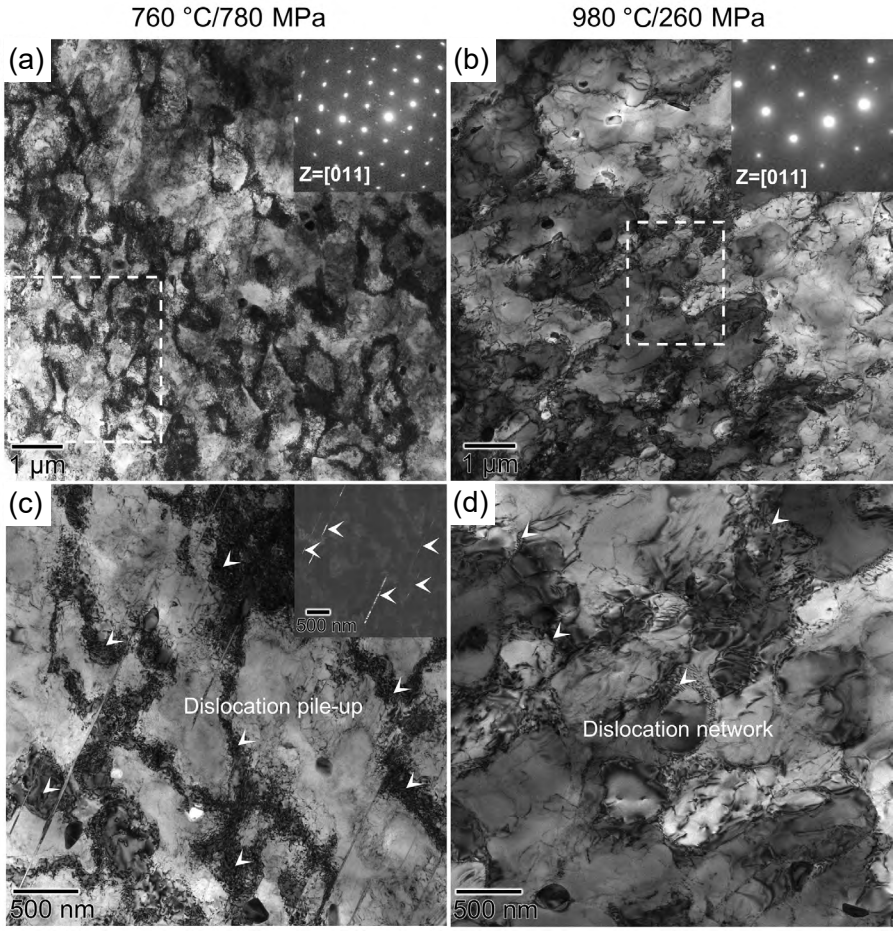

Fig. 8: Deformation microstructure of CLM after stress rupture test with both conditions: (a, c) 760 °C/780 MPa; (b, d) 980 °C/260 MPa

dislocation network around the γ′ phase, therefore, whereas conventional superalloys are optimized by increasing the content and strength of the γ′ phase (such as single crystals), in CLM, the focus is on the elimination of transverse grain boundaries within <110> grains.

4 Conclusions

In this study, the ZGH451 superalloy with crystallographic lamellar microstructure (CLM) was fabricated by LPBF, and the effect of CLM on the stress rupture performance at 760 °C/780 MPa and 980 °C/260 MPa was investigated. The stress rupture life and fracture mechanism were thoroughly examined using SEM, EBSD, and TEM. The evolution mechanisms of intergranular cracking, precipitated phase, and defects were discussed. The main conclusions are summarized as follows:

(1) The CLM after HIP primarily consists of lamellar grains, including <001>//BD and <110>//BD oriented grains. A flatness keyhole shape melt pool provides a favorable heat flux condition for CLM. These non-CLM grains (stray grains) derive from heat flow fluctuation, resulting in the evolution of high-angle transverse grain boundaries. Moreover, the HIP treatment promotes the precipitation and coarsening of the γ′ phase, and these processes accumulate a large number of early dislocations.

(2) The alloy test at 980 °C/260 MPa exhibits higher plasticity and lower stress-rupture life. Through combined observation of the transversal and longitudinal sections of the fracture, high temperature-induced intergranular fracture is identified as the primary cause of the low-stress rupture life under the 980 °C/260 MPa condition. For the alloy at 760 °C/780 MPa, there is only one long stripe crack with several microcracks around. Therefore, the sub-grains and transgranular fracture dominate failure and consequently increasing the life value.

(3) The stress-rupture microstructure reveals that deformation twins are prevalent in <110>//BD-oriented grains under both 760 °C/780 MPa and 980 °C/260 MPa conditions. The evolution of the dislocation network and associated interaction with other defects enhance plastic deformation capabilities of the alloy at 980 °C/260 MPa. In addition, the wider γ′ phase dimensions and narrower γ channel facilitate dislocation slip and benefit the plasticity of CLM in 980 °C/260 MPa.

Acknowledgments

The authors gratefully acknowledge the financial support by the Project of Taihang Laboratory (No. A3023) and Science Center for Gas Turbine Project (Grant No. P2022-C-IV-002-001).

Conflict of interest

The authors declare that they have no known competing financial interests or personal relationships that could have appeared to influence the work reported in this paper.

References

[1] Qi X H, Liang X K, Wang J H, et al. Microstructure tailoring in laser powder bed fusion (L-PBF): Strategies, challenges, and future outlooks. Journal of Alloys and Compounds, 2024, 970: 9702024. https://doi.org/10.1016/j.jallcom.2023.172564

[2] Tang Y T, Panwisawas C, Ghoussoub J N, et al. Alloys-by-design: Application to new superalloys for additive manufacturing. Acta Materialia, 2021, 202: 417–436. https://doi.org/10.1016/j.actamat.2020.09.023

[3] An D Y, Zhou Y H, Liu X X, et al. Exploring structural origins responsible for the exceptional mechanical property of additively manufactured 316L stainless steel via in-situ and comparative investigations. International Journal of Plasticity, 2023, 170: 103769. https://doi.org/10.1016/j.ijplas.2023.103769

[4] Andreau O, Koutiri I, Peyre P, et al. Texture control of 316L parts by modulation of the melt pool morphology in selective laser melting. Journal of Materials Processing Technology, 2019, 264: 21–31. https://doi.org/10.1016/j.jmatprotec.2018.08.049

[5] Mayama T, Ishimoto T, Tane M, et al. Novel strengthening mechanism of laser powder bed fusion-manufactured Inconel 718: Effects of customized hierarchical interfaces. Additive Manufacturing, 2024, 93: 104412. https://doi.org/10.1016/j.addma.2024.104412

[6] Yao L M, Xiao Z M, Hoo Z S, et al. Mechanism analysis of grain growth dominated by alloy composition gradients during powder bed fusion. Materials Research Letters, 2023, 11(10): 814–820. https://doi.org/10.1080/21663831.2023.2250826

[7] Dang X F, Li Y, Chen K, et al. Avoiding cracks in additively manufactured non-weldable directionally solidified Ni-based superalloys. Additive Manufacturing, 2022, 59: 592022. https://doi.org/10.1016/j.addma.2022.103095

[8] Titus M S, Eggeler Y M, Suzuki A, et al. Creep-induced planar defects in L12-containing Co- and CoNi-base single-crystal superalloys. Acta Materialia, 2015, 82: 530–539. https://doi.org/https://doi.org/10.1016/j.actamat.2014.08.033

[9] Wang P, Liang J J, Zhu Y P, et al. Pursued strength-ductility synergy in Ni superalloys produced by laser powder bed fusion: Crystallographic lamellar versus directionally solidified microstructure. Materials Science and Engineering: A, 2025, 925: 147838. https://doi.org/https://doi.org/10.1016/j.msea.2025.147838

[10] Gokcekaya O, Hayashi N, Ishimoto T, et al. Crystallographic orientation control of pure chromium via laser powder bed fusion and improved high temperature oxidation resistance. Additive Manufacturing, 2020, 36: 101624. https://doi.org/10.1016/j.addma.2020.101624

[11] Enrique P D, Minasyan T, Toyserkani E. Laser powder bed fusion of difficult-to-print γ′ Ni-based superalloys: A review of processing approaches, properties, and remaining challenges. Additive Manufacturing, 2025, 106: 104811. https://doi.org/10.1016/j.addma.2025.104811

[12] Sofinowski K A, Raman S, Wang X G, et al. Layer-wise engineering of grain orientation (LEGO) in laser powder bed fusion of stainless steel 316L. Additive Manufacturing, 2021, 38: 101809. https://doi.org/10.1016/j.addma.2020.101809

[13] Wang X Y, Cao M Y, Zhao Y, et al. Microstructural causes and mechanisms of crack growth rate transition and fluctuation of additively manufactured titanium alloy. International Journal of Plasticity, 2024, 179: 104034. https://doi.org/10.1016/j.ijplas.2024.104034

[14] Song W, Yang J Y, Liang J J, et al. A new approach to design advanced superalloys for additive manufacturing. Additive Manufacturing, 2024, 84: 104098. https://doi.org/10.1016/j.addma.2024.104098

[15] Tsutsumi Y, Ishimoto T, Oishi T, et al. Crystallographic texture- and grain boundary density-independent improvement of corrosion resistance in austenitic 316L stainless steel fabricated via laser powder bed fusion. Additive Manufacturing, 2021, 45: 102066. https://doi.org/10.1016/j.addma.2021.102066

[16] Yao L M, Huang S, Ramamurty U, et al. On the formation of “Fish-scale” morphology with curved grain interfacial microstructures during selective laser melting of dissimilar alloys. Acta Materialia, 2021, 220: 117331. https://doi.org/10.1016/j.actamat.2021.117331

[17] Yao L M, Xiao Z M, Ramesh A, et al. On the melt pool flow and interface shape of dissimilar alloys via selective laser melting. International Communications in Heat and Mass Transfer, 2023, 145: 106833. https://doi.org/10.1016/j.icheatmasstransfer.2023.106833

[18] Wang Y N, Wang B B, Luo L S, et al. Build atmosphere aided texture control in additively manufactured FeCrAl steel by laser powder bed fusion. Scripta Materialia, 2024, 239: 115806. https://doi.org/10.1016/j.scriptamat.2023.115806

[19] Yang X L, Gibbons G J, Tanner D A, et al. Scan strategy induced microstructure and consolidation variation in the laser-powder bed fusion (L-PBF) additive manufacturing of low alloy 20MnCr5 steel. Materials & Design, 2023, 232: 112160. https://doi.org/10.1016/j.matdes.2023.112160

[20] He X Y, Wang H, Liao X Z, et al. Nano-twining and deformation-induced martensitic transformation in a duplex stainless steel 2205 fabricated by laser powder bed fusion. Additive Manufacturing, 2024, 84: 104110. https://doi.org/10.1016/j.addma.2024.104110

[21] Freund L P, Messé O M D M, Barnard J S, et al. Segregation assisted microtwinning during creep of a polycrystalline $L1_2$-hardened Co-base superalloy. Acta Materialia, 2017, 123: 295–304. https://doi.org/10.1016/j.actamat.2016.10.048

[22] Neumeier S, Freund L P, Göken M. Novel wrought γ/γ′ cobalt base superalloys with high strength and improved oxidation resistance. Scripta Materialia, 2015, 109: 104–107. https://doi.org/https://doi.org/10.1016/j.scriptamat.2015.07.030

[23] Li N, Wang Q, Bermingham M, et al. Tensile properties and microstructural evolution of 17-4 PH stainless steel fabricated by laser hybrid additive manufacturing technology. International Journal of Plasticity, 2024, 173: 103885. https://doi.org/10.1016/j.ijplas.2024.103885

[24] Bajaj D, Chen Z, Qu S J, et al. Distinct origins of deformation twinning in an additively-manufactured high-entropy alloy. Additive Manufacturing, 2023, 74: 03716. https://doi.org/10.1016/j.addma.2023.103716

[25] Ahmad N, Ghiaasiaan R, Gradl P R, et al. Revealing deformation mechanisms in additively manufactured alloy 718: Cryogenic to elevated temperatures. Materials Science and Engineering: A, 2022, 849: 143528. https://doi.org/10.1016/j.msea.2022.143528